

PAPER • OPEN ACCESS

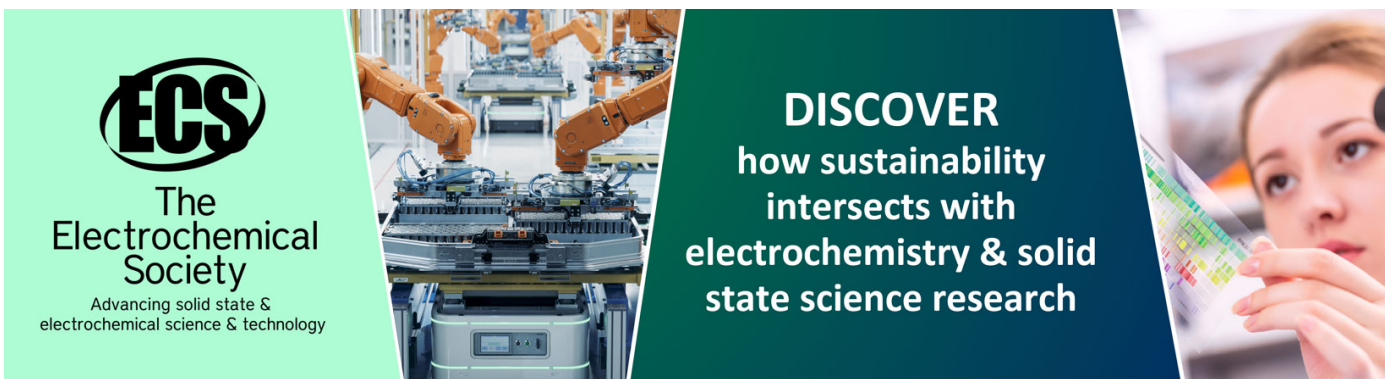
# Reconfigurable screen-printed terahertz frequency selective surface based on metallic checkerboard pattern

To cite this article: Redwan Ahmad *et al* 2024 *Flex. Print. Electron.* **9** 025005

View the [article online](#) for updates and enhancements.

You may also like

- [THE DARK ENERGY CAMERA](#)  
B. Flaugher, H. T. Diehl, K. Honscheid et al.
- [Effective Reduction in Crosstalk Effects in Quaternary Integrated Circuits Using Mixed Carbon Nanotube Bundle Interconnects](#)  
Mohammad Hossein Moaiyeri, Zahra Hajmohammadi, Maryam Rezaei Khezeli et al.
- [Design, modeling and experimental validation of a micro cantilever beam with an electro-controllable twisting ability](#)  
Xiaoyu Su, Zhongjing Ren, Quan Pan et al.



**ECS**  
The Electrochemical Society  
Advancing solid state & electrochemical science & technology

**DISCOVER**  
how sustainability intersects with electrochemistry & solid state science research

# Flexible and Printed Electronics



## PAPER

# Reconfigurable screen-printed terahertz frequency selective surface based on metallic checkerboard pattern

### OPEN ACCESS

RECEIVED  
29 December 2023

REVISED  
26 February 2024

ACCEPTED FOR PUBLICATION  
8 April 2024

PUBLISHED  
18 April 2024

Redwan Ahmad<sup>1</sup> , Xavier Ropagnol<sup>1,2</sup>, Ngoc Duc Trinh<sup>3</sup> , Chloé Bois<sup>3</sup> and François Blanchard<sup>1,\*</sup> 

<sup>1</sup> Département de génie électrique, École de technologie supérieure (ÉTS), Montréal QC H3C 1K3, Canada

<sup>2</sup> Institut national de la recherche scientifique, EMT research center, Varennes QC J3X 1P7, Canada

<sup>3</sup> Institut des communications graphiques et de l'imprimabilité, Montréal QC H2M 2E2, Canada

\* Author to whom any correspondence should be addressed.

E-mail: [francois.blanchard@etsmtl.ca](mailto:francois.blanchard@etsmtl.ca)

**Keywords:** screen-printing, metallic checkerboard, terahertz, reconfigurable frequency selective surface

Original content from this work may be used under the terms of the

[Creative Commons Attribution 4.0 licence](https://creativecommons.org/licenses/by/4.0/).

Any further distribution of this work must maintain attribution to the author(s) and the title of the work, journal citation and DOI.



## Abstract

We employed the screen-printing method to fabricate terahertz (THz) frequency selective surfaces (FSSs) featuring an inductive metallic checkerboard (i-MCB) pattern based on conductive silver ink onto a flexible polyethylene terephthalate substrate, chosen for its excellent THz transmission properties below 1 THz [Jin *et al* 2006 *J. Korean Phys. Soc.* **49** 513–17]. Analytical studies, along with simulations and experiments, were conducted to investigate the filtering characteristics of the printed FSSs, confirming their functionality as a band-pass filter. Subsequently, we demonstrated the reconfigurability of a two-layer system by vertically stacking two layers. This was achieved by systematically shifting the position of the second layer in the  $x$  or  $y$ -direction relative to the first layer. Experimental verification revealed a significant variation in normalized transmission, ranging from 94% to 6% at 0.15 THz for type-I:i-MCBs and 90% to 5% at 0.20 THz for type-II:i-MCBs, respectively. This study presents a simple scheme for a reconfigurable screen-printed i-MCB-FSS operating in the THz range. Consequently, our findings demonstrate that screen printing method can effectively be employed for the large-scale production of THz FSSs.

## 1. Introduction

To enhance the diversity of terahertz (THz) applications, there is a growing demand for the development and production of THz optics, encompassing polarizers [1], filters [2], absorbers [3], phase shifters [4], wave plates [5], and more. In this context, frequency-selective surfaces (FSSs) play a crucial role. These thin, periodic structures, composed of both conductive and non-conductive materials and generally exhibiting features on the order of the wavelength size, are capable of transmitting or reflecting electromagnetic waves at specific frequencies [6]. Their versatility has led to extensive applications in manipulating THz waves, including polarization conversion [7], transmission measurement in quasi-optical systems [8], remote sensing [9], monochrometers [10], and more. For more adaptive solutions, there has been a surge in demand for reconfigurable frequency-selective surfaces (RFSSs) in various applications, including frequency agility, beam

steering, polarization control, and dynamic filtering [11–13]. In the microwave regions, distinct FSSs and RFSSs have long been demonstrated [14–18]. The reconfigurability of these devices generally involves a large variety of tuning mechanisms, encompassing thermal tuning [14], rotational tuning [15], electrical tuning [16, 17], mechanical tuning [18], water-based metamaterial absorbers [19, 20], and more. In the THz region, RFSSs have recently found applications using various tuning approaches, including a polarizer based on vanadium dioxide [12], a mechanically tunable filter using a polydimethylsiloxane substrate [21], modulators based on FSS-graphene stacked structures [22], a mechanically reconfigurable bandpass filter [23], electronically controlled flexible THz modulator [24], and thermally tunable FSS based on barium strontium titanate thin film and metamaterials [25]. Numerous fabrication techniques, including photolithography [12, 22], milling [8], and laser ablation [26], have been employed for THz FSS fabrication, each chosen based on design

requirements and materials. Despite their precision, these methods are time-consuming, expensive, and limited to small-scale production.

In the recent years, printable electronics (PE) pop up as an alternative solution for the fabrication of THz devices [27–30]. The advantages of PE include mass production capability with low cost per unit, good reproducibility, and more eco-friendly production [31]. This process requires only three steps: selection of the right substrate and ink; printing the pattern upon the substrate; and sintering. Because of their high conductivity and low loss, conductive inks including copper, graphene, and others, are widely employed to transfer the pattern upon the flexible plastic substrate. The main PE-based fabrication technologies are flexography printing, hot-stamping, screen-printing, and ink-jet printing [32, 33]. Despite the relatively low resolution of the printed pattern, which is in the order of a few tens of microns, printing THz devices with features on the order of the wavelength size remains adequate. Consequently, PE is highly suitable for the fabrication of THz FSS. Examples of printed THz devices include a band-pass filter [28], vortex phase plate [29], and polarizer [30]. More recently, a printed reconfigurable flexible FSS has been demonstrated based on the Moiré interference technique [28]. To date, printed THz devices have been created exclusively through ink-jet printing, flexography, or hot stamping techniques. In contrast, the screen-printing method has been solely employed for the fabrication of devices within the microwave frequency range [34–36].

In this work, we demonstrate the design, simulation, fabrication, and characterization of THz FSSs based on metallic checkerboard patterns (MCB) using screen printing as the fabrication technique. The analyzed FSS pattern is printed on a polyethylene terephthalate (PET) substrate with conductive silver (Ag) ink (CXT-0657). A polarization dependent reconfigurability is achieved by stacking two identical FSS layers and shifting the second layer relative to the position of the first layer. Notably, this reconfigurability is obtained without employing any external stimuli such as biasing voltage, temperature variation, or external continuous wave (CW) laser. Consistent with our simulations, experimental results reveal a maximum variation in transmission, ranging from 94% to 6% at a center frequency of 0.150 THz.

## 2. Methodology

### 2.1. Modeling and design of FSS

Being a complementary structure, MCB patterns have long been the subject of extensive studies in various fields of application [37–44]. According to Babinet's principle, the complementary structure of an obstacle (or object) presents complementary transmission spectra [45]. In the geometry of an ideal MCB, square metallic blocks are connected without any

gap, as illustrated in figure 1(a), behaving as a half-beam splitter. When the square non-metallic block is reduced in size compared to its metallic counterpart, creating an asymmetric structure, we define a separation distance  $\Delta d$  relative to its physical dimensions ( $x$ ,  $y$ , and  $\Delta z$ ), as illustrated in figure 1(b). This specific case has been termed as inductive MCB (i-MCB) [38, 39]. On the contrary, when the square metallic parts are smaller than their counterparts, we define it as capacitive MCB (c-MCB). The schematic of i-MCB and c-MCB pattern is represented in figures 1(c) and (d), respectively. The corresponding reactances ( $X_{in}$  and  $X_{cap}$ ) of the i-MCB and c-MCB are described by parallel and series combinations of inductances and capacitances [40]. See their electrical representations in figures 1(e) and (f), respectively. Here,  $Z_0$  represents the impedance of free space, and  $n$  is the refractive index of the substrate. The resistivity ( $R$ ) in the circuit models is neglected since the analysis assumes a low-loss conductor. The transmittance ( $T$ ) could be calculated as follows [40]:

$$T_j = \frac{4nX_j^2}{1 + (1+n)^2X_j^2} \text{ where } j = \text{in, cap.} \quad (1)$$

The reactance  $X_{in}$  of the parallel resonant circuit ( $L_{in}$ ,  $C_{in}$ ) and  $X_{cap}$  of the series resonant circuit ( $L_{cap}$ ,  $C_{cap}$ ) can be defined as [40]:

$$X_{in} = \frac{\omega L_{in}}{1 - \omega^2 L_{in} C_{in}} \quad (2)$$

$$X_{cap} = \frac{\omega^2 L_{cap} C_{cap} - 1}{\omega C_{cap}}. \quad (3)$$

For the limit  $\omega \rightarrow 0$ ,  $X_{in}$  and  $X_{cap}$  become 0 and  $\infty$ . Based on their connection states among metal squares i.e., overlapped (i-MCB) or disconnected (c-MCB), the electromagnetic responses of the MCB FSS behave as band-pass and band-stop filter respectively. Furthermore, the peak transmission frequency ( $f_{peak}$ ) of the i-MCB can be predicted using the following equation [37]:

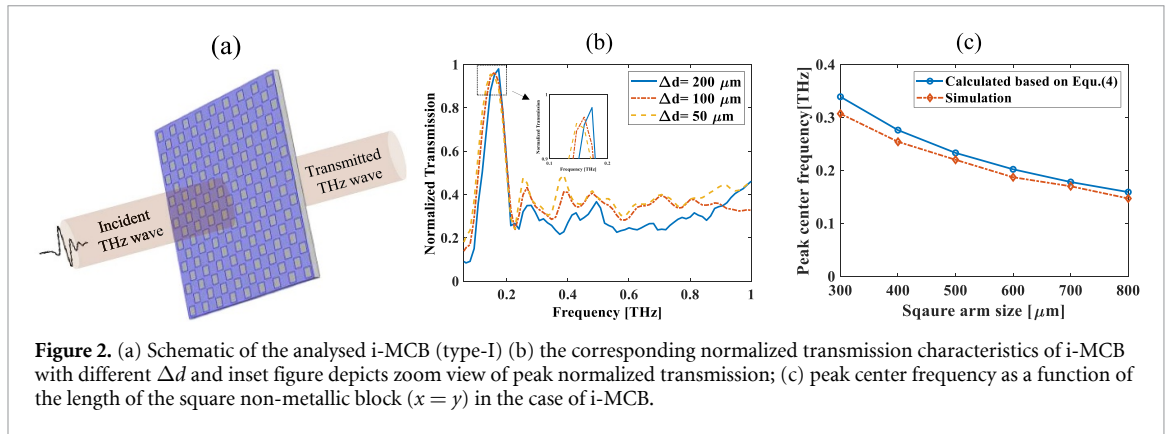
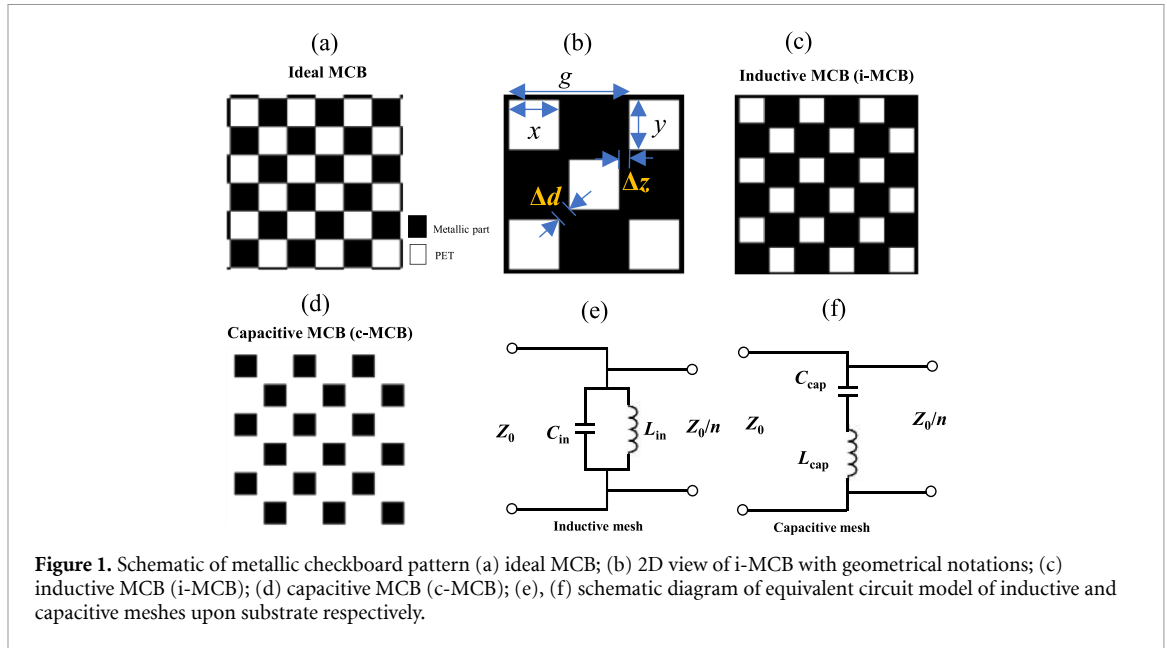
$$f_{peak} = \frac{c}{g} \quad (4)$$

where  $c$  is the speed of light and  $g$  is defined as  $g = 2(x + \Delta z)$ . Also,  $\Delta z$  is related as  $\Delta z = \frac{\Delta d}{\sqrt{2}}$ .

In the following analysis, we have carried out finite-difference time-domain (FDTD) simulations from Ansys Lumerical software to evaluate the transmission characteristics of i-MCBs and c-MCBs. Furthermore, the normalized transmission (NT) was calculated using equation (5):

$$NT(\omega) = \left| \frac{T_{sample}(\omega)}{T_{ref}(\omega)} \right| \quad (5)$$

where  $T_{Sample}(\omega)$  and  $T_{Ref}(\omega)$  are the transmission coefficient of the sample and reference (substrate), respectively [28].



Schematic of the i-MCB FSS with the operational principle is depicted in figure 2(a), where purple and gray colors denote the metallic and PET part, respectively. The simulated transmission characteristics of i-MCB for different  $\Delta d$  are presented in figure 2(b) and confirmed that the i-MCB behaves as expected, acting like a band-pass filter [38]. The center frequency increases as the non-conductive zone shrinks, from 0.150 THz to 0.173 THz. Only a slight difference is noticed in the transmission characteristics when  $\Delta d$  is increased, which is explained by the smaller total open aperture of the filter. Conversely, although not shown here, c-MCB behaves like a band-stop filter [38]. As depicted in figure 2(c), it is evident that increasing the length of the square hole ( $x$ ) while maintaining a fixed gap  $\Delta d$  of 200  $\mu\text{m}$  gradually reduces the corresponding peak center frequency. Essentially, the peak center frequency of the i-MCB can be shifted to the higher or lower portion of the THz region by decreasing or increasing the lattice of the square pattern of MCB, respectively.

For all subsequent transmission analyses of the i-MCB structure using our simulation tool or experimentally, we maintained a constant  $\Delta d$  of 200  $\mu\text{m}$ . We investigated two i-MCB structures with different lattice sizes: type-I with square block dimensions of  $700 \times 700 \mu\text{m}^2$  and type-II with square block dimensions of  $500 \times 500 \mu\text{m}^2$ .

## 2.2. Fabrication of THz FSS and experimental setup

FSS's pattern was printed upon a plastic substrate using silver ink utilizing a screen-printing technology (EKRA X1-SL Semi-Automatic Screen Printer) [36]. Though we have used a flat-bed screen printing system as a fabrication tool, both flexible and rigid substrates could be employed to print upon it. However, in this work as a substrate, widely used low-cost PET has been chosen due to having excellent THz transmission properties as well as mechanical properties, including strength, flexibility, etc. Correspondingly, the thickness of the PET substrate is 125  $\mu\text{m}$  and the properties of the used substrate

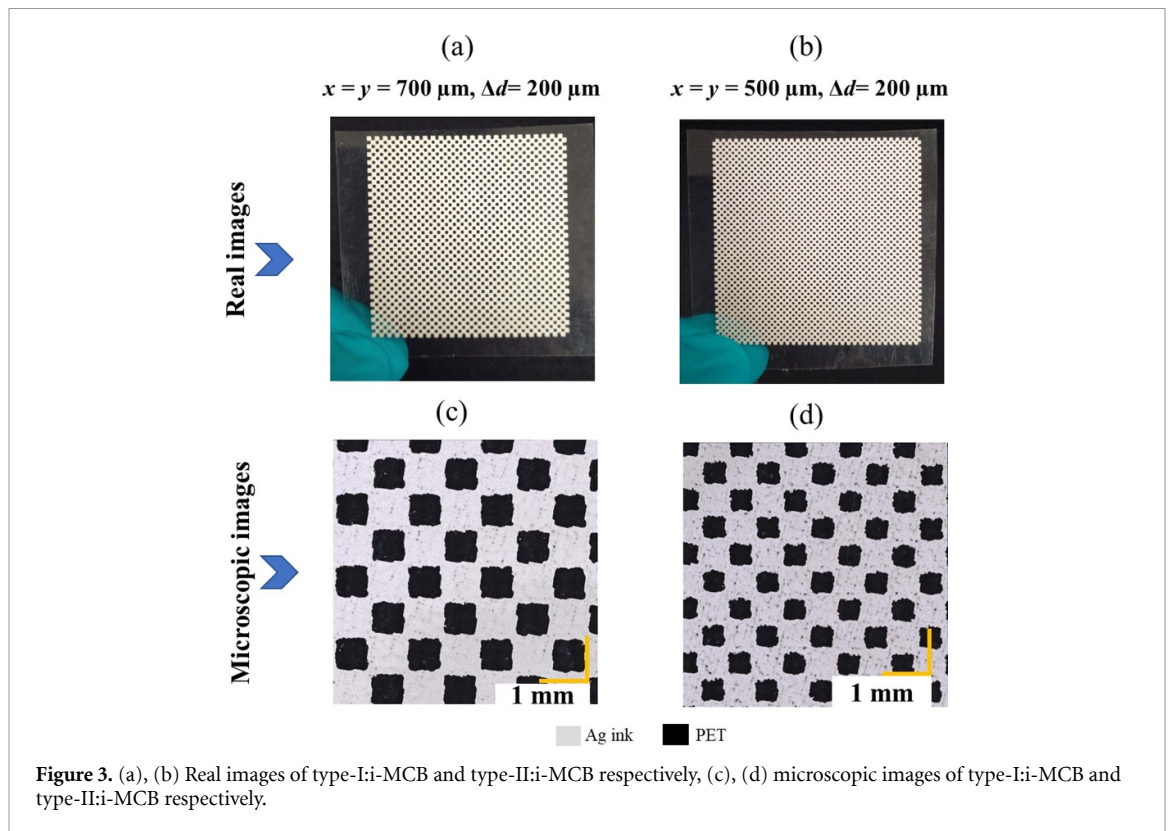


**Figure 3.** (a), (b) Real images of type-I-i-MCB and type-II-i-MCB respectively, (c), (d) microscopic images of type-I-i-MCB and type-II-i-MCB respectively.

can be found in [46]. Consequently, analyzed MCBs were printed and cured in the oven with hot air at a temperature of  $90^\circ\text{C}$ . The resulting sample had a thickness of  $\sim 2 \mu\text{m}$  and conductivity measured as  $5.0 \times 10^6 \text{ S m}^{-1}$  using the 4-point probe method. The fabricated sample of type-I&II: i-MCB has the following dimensions: square non-metallic part was  $\sim 700 \times 700 \mu\text{m}^2$  and  $\sim 500 \times 500 \mu\text{m}^2$  respectively and in both cases the distance between diagonally cornered two square blocks,  $\Delta d$  as  $\sim 200 \mu\text{m}$ . The sample was 40 mm in length by 40 mm in width as dimension. The microscopic images of the fabricated MCBs are shown in figure 3. Microscopic images were taken on a digital microscope (Model: Keyence VHX-7000). From microscopic images, it is evident that some irregularities on edges are noticeable in the square non-metallic block shapes due to ink spreading, which is typical for the screen-printing method [32].

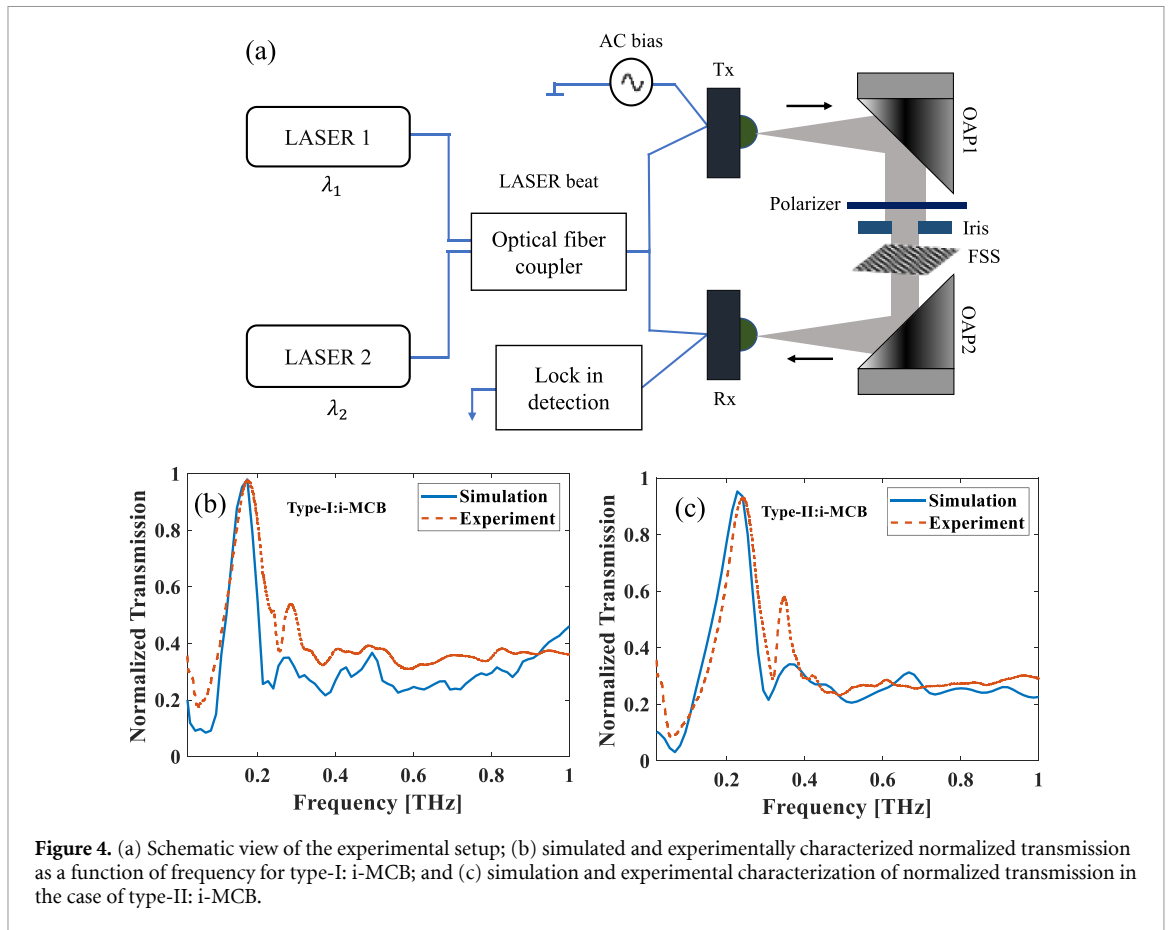
To validate the simulation results and experimentally examine the transmission features of the fabricated FSSs, we utilized a commercial CW THz spectroscopy system (TOPTICA photonics' TERASCAN 1550). The experimental setup is illustrated in figure 4(a). The THz emitter and receiver are based on the InGaAs photodiode and InGaAs photomixer respectively. The THz waves were collimated and refocused onto the detector using a pair of off-axis parabolic (OAP) mirrors, with a 2-inch grid polarizer ensured linear polarization of the incident THz wave. Additionally, an iris was employed just before the sample holder to control the beam size,

making it compatible with the sample dimensions. It is important to note that, in our experiment, we utilized a resolution of 50 MHz to discern the characteristics of our band-pass filters.

### 3. Results and discussion

#### 3.1. Single layer of FSS

The center frequencies were calculated by equation (4) for the two i-MCB structures, i.e. type-I and type-II, which are 0.178 THz and 0.233 THz respectively. Following this prediction, the NT of the two samples was evaluated by simulation and experimentally. Figures 4(b) and (c) show the results of the simulation and experimental analysis of our two sample types. A simulated transmission peak ( $f_{\text{peak}}$ ) at 0.173 THz and 0.226 THz is obtained, whereas the experimental transmission peaks are 0.180 THz and 0.243 THz for type-I and II samples, respectively, in perfect agreement with the previous calculation. It is noticeable that, as the size of the square non-metallic block ( $x$ ) is reduced from  $700 \mu\text{m}$  to  $500 \mu\text{m}$ , the corresponding peak transmission frequency is shifted towards higher frequency with a very small transmission reduction from 98% to 96%. Both types of i-MCB behave as band-pass filters, exhibiting simulated bandwidths of 100 GHz and 110 GHz, and experimental bandwidths of 125 GHz and 120 GHz for types I and II, respectively. These results show good agreement between the simulated and experimental data. Experimentally obtained NT in both



types of i-MCB are also consistent with the simulation results with insignificant variances.

### 3.2. Reconfigurability of FSS

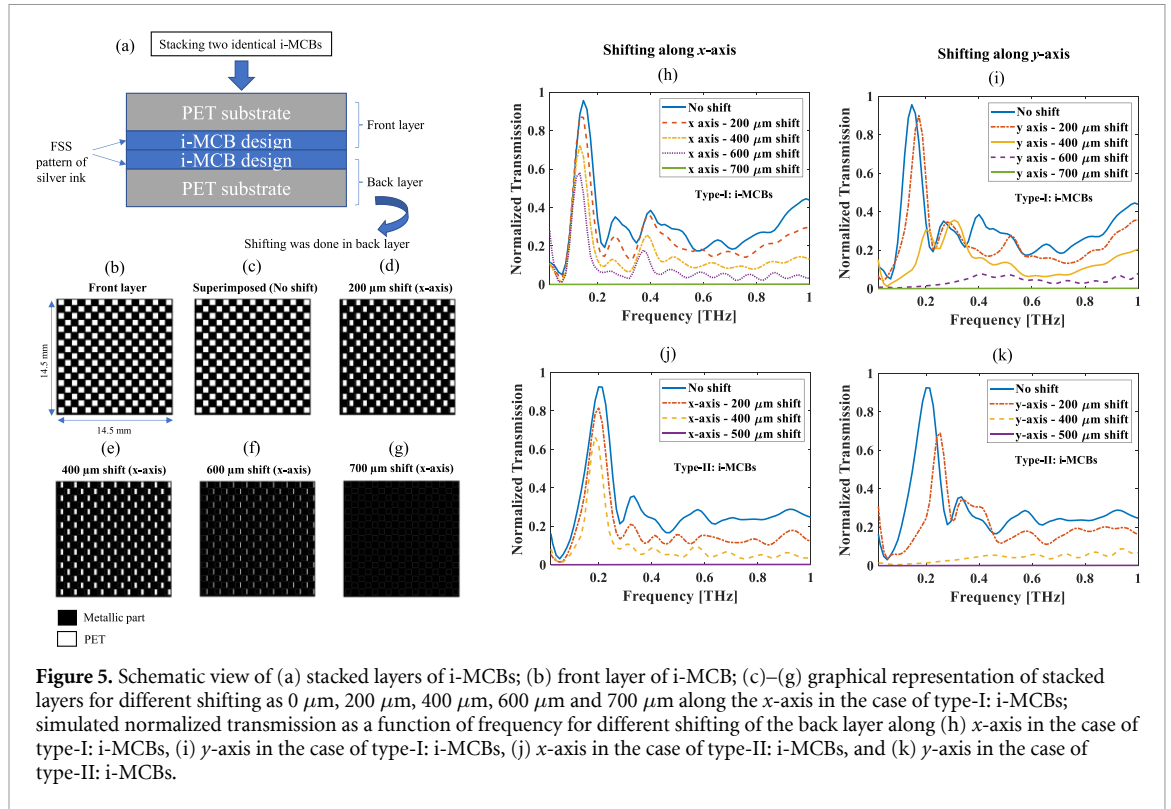
#### 3.2.1. Simulation analysis

To achieve reconfigurability, we used two identical MCB layers, one of which is movable relative to the second. The aim of this reconfigurability is to maximize transmission variation without affecting filter frequency or spectral width. For this purpose, two identical layers of i-MCB (front and back layer) have been superimposed (figure 5(a)), and shifting was done on the back layer along the  $x$  or  $y$ -axis to obtain the reconfigurability. Shifting was performed along the  $x$ -axis from  $0 \mu\text{m}$  to  $700 \mu\text{m}$  in the case of type-I i-MCBs, as illustrated in figures 5(c)–(g). Similarly, in the case of type-II i-MCBs, shifting was done from  $0$  to  $500 \mu\text{m}$  (figures not shown here). Observing figures 5(c)–(g), it is evident that shifting the back layer increases the conductive area as well as the distance between the corner edges of two non-metallic blocks of the stacked layers ( $\Delta d_{\text{stacked}}$ ). With a shift of  $700 \mu\text{m}$ , a fully conductive pattern is formed, capable of blocking or reflecting incoming THz waves.

FDTD simulations were conducted to characterize the reconfigurable i-MCB FSS. In figure 5(h), it is observed that for the case of type-I i-MCB, shifting along the  $x$ -axis from  $0 \mu\text{m}$  to  $700 \mu\text{m}$  produces

a NT change from 95% to almost 0% at the peak frequency of  $0.146 \text{ THz}$ . Note that the polarization direction of the incoming THz beam is set linearly in the  $x$ -direction. It is noteworthy that both the non-shifted pattern and the pattern shifted by  $700 \mu\text{m}$  exhibit polarization insensitivity due to their symmetrical shapes. Conversely, the patterns shifted by  $200 \mu\text{m}$ ,  $400 \mu\text{m}$ , and  $600 \mu\text{m}$  are polarization-sensitive, given their rectangular configurations. To assess the impact of polarization, we analyzed the corresponding NT for shifting along the  $y$ -axis at  $0 \mu\text{m}$ ,  $200 \mu\text{m}$ ,  $400 \mu\text{m}$ ,  $600 \mu\text{m}$ , and  $700 \mu\text{m}$ .

In figure 5(i), the transmission at the peak frequency of  $0.146 \text{ THz}$  shows a distinct difference for changes along the  $y$  direction compared to changes along the  $x$  direction. While the transmission tends to remain stable, it suddenly attenuates, indicating a lack of precise control of the peak transmission when shifting in the opposite direction to the THz wave polarization. More specifically, a noticeable difference emerges along the  $x$  and  $y$  axis, particularly for type-II: i-MCBs, shifts along the  $x$ -axis ( $0 \mu\text{m}$ ,  $200 \mu\text{m}$ ,  $400 \mu\text{m}$ , and  $500 \mu\text{m}$ ) produce NTs of 92%, 80%, 65%, and 0%, respectively at  $0.195 \text{ THz}$  (figure 5(j)). By contrast, shifting along the  $y$ -axis cannot be evaluated, as the peak shifts slightly to a higher frequency and suddenly disappears at an offset of  $400 \mu\text{m}$  (figure 5(k)).



To evaluate the performances of the proposed THz reconfigurable FSS, the variation in NT needed to be calculated for various shifting along the  $x$  or  $y$ -axis at the operating frequency. The operating frequency ( $f_{\text{opt}}$ ) is calculated as the peak center frequency when the back layer of two i-MCBs is not shifted i.e. 0  $\mu\text{m}$  shift along the  $x$  or  $y$ -axis. The variation in NT is defined as follows:

$$\text{Variation (\%)} = \left| T_{0\mu\text{m}(f_{\text{opt}})} - T_{x\mu\text{m}(f_{\text{opt}})} \right| \times 100\% \quad (6)$$

where  $T_{0\mu\text{m}(f_{\text{opt}})}$  and  $T_{x\mu\text{m}(f_{\text{opt}})}$  are the NT of the 0  $\mu\text{m}$  and  $x$   $\mu\text{m}$  shift along the  $x$  or  $y$ -axis, respectively, at the operating frequency ( $f_{\text{opt}}$ ). The variation in NT has been calculated based on the simulation results for both types of i-MCBs. It is noticeable that type-I: i-MCBs exhibit maximum variation in NT as of  $\sim 95\%$  at 0.146 THz for 700  $\mu\text{m}$  shifting irrespective of the  $x$  or  $y$ -axis with reference to no shifted pattern whereas type-II: i-MCBs exhibit maximum variation in NT as of  $\sim 92\%$  at 0.195 THz for 500  $\mu\text{m}$  shifting.

Next, we explored the effects of superimposing two layers of type-I: c-MCB. Shifting was applied along both the  $x$  and  $y$ -axis at a fixed distance. The resulting simulated images, illustrating the movement along the  $x$ -axis, are presented in figures 6(a)–(e). The metallic component progressively grows as the shift occurs along the  $x$ -axis. Notably, achieving a complete metallic coverage, as observed in the case of i-MCB, is unattainable with the c-MCB, see figures 6(a)–(e).

Consequently, this scenario results in a square lattice FSS when the back layer of c-MCBs is shifted along the  $x$  or  $y$ -axis by approximately 840  $\mu\text{m}$ .

The simulation analysis considered various shifts along the  $y$ -axis, including 0  $\mu\text{m}$ , 200  $\mu\text{m}$ , 400  $\mu\text{m}$ , 600  $\mu\text{m}$ , and 840  $\mu\text{m}$ , as depicted in figure 6(f). In figure 6(f), it is observed that the notch frequency of the corresponding band-stop filter progressively shifts to higher frequencies as the  $y$ -axis undergoes a gradual shift from 0  $\mu\text{m}$  to 840  $\mu\text{m}$ . The resulting notch frequencies are 0.146 THz, 0.174 THz, 0.186 THz, 0.213 THz, and 0.280 THz for shifts of 0  $\mu\text{m}$ , 200  $\mu\text{m}$ , 400  $\mu\text{m}$ , 600  $\mu\text{m}$ , and 840  $\mu\text{m}$ , respectively. Additionally, under no-shift conditions, the corresponding NT is 18.8%, while for an 840  $\mu\text{m}$  shift, it decreases to 3.34%. Similarly, as the shift occurred toward the  $x$ -axis, the notch frequency gradually shifted towards the lower frequency range (see figure 6(g)). The associated notch frequencies are 0.133 THz, 0.120 THz, and 0.106 THz for shifts of 200  $\mu\text{m}$ , 400  $\mu\text{m}$ , and 600  $\mu\text{m}$ , respectively. Notably, the notch frequency for both no shift and an 840  $\mu\text{m}$  shift towards the  $x$ -axis remains unchanged compared to the  $y$ -axis shift, owing to the polarization-insensitive symmetrical structure. However, for both cases of  $x$  and  $y$  shift, this reduction in transmission comes with the trade-off of significant broadband attenuation, meaning that there is nearly no transmission of the THz beam through the filter when the two layers completely overlap. Also, from figure 6(h) it is evident that, the spectral responses of the stacked layers of c-MCBs were not fulfilling the aims of this

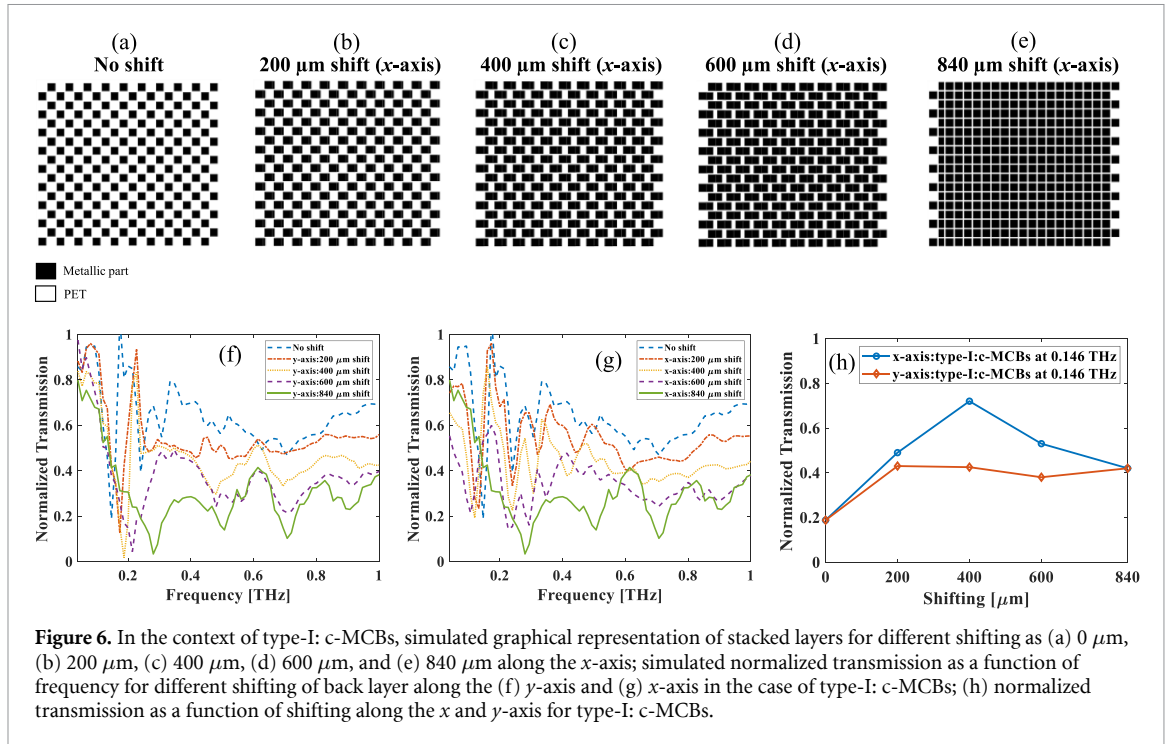


**Figure 6.** In the context of type-I: c-MCBs, simulated graphical representation of stacked layers for different shifting as (a) 0  $\mu\text{m}$ , (b) 200  $\mu\text{m}$ , (c) 400  $\mu\text{m}$ , (d) 600  $\mu\text{m}$ , and (e) 840  $\mu\text{m}$  along the  $x$ -axis; simulated normalized transmission as a function of frequency for different shifting of back layer along the (f)  $y$ -axis and (g)  $x$ -axis in the case of type-I: c-MCBs; (h) normalized transmission as a function of shifting along the  $x$  and  $y$ -axis for type-I: c-MCBs.

proposed method to be performed as a reconfigurable FSS. Correspondingly it is seen that, the variation in NT at 0.146 THz is not noteworthy as compared to i-MCBs. Due to this, the c-MCB was deemed less appealing as a reconfigurable FSS in terms of variation in NT at  $f_{\text{opt}}$  and only i-MCBs were explored experimentally.

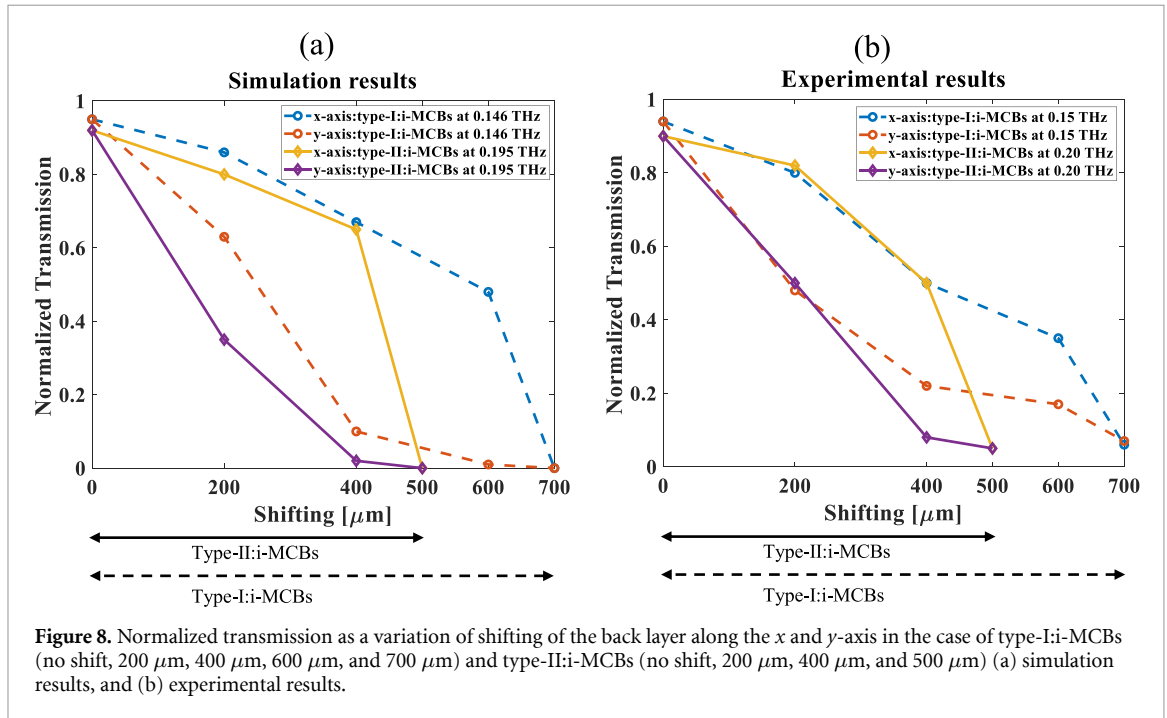
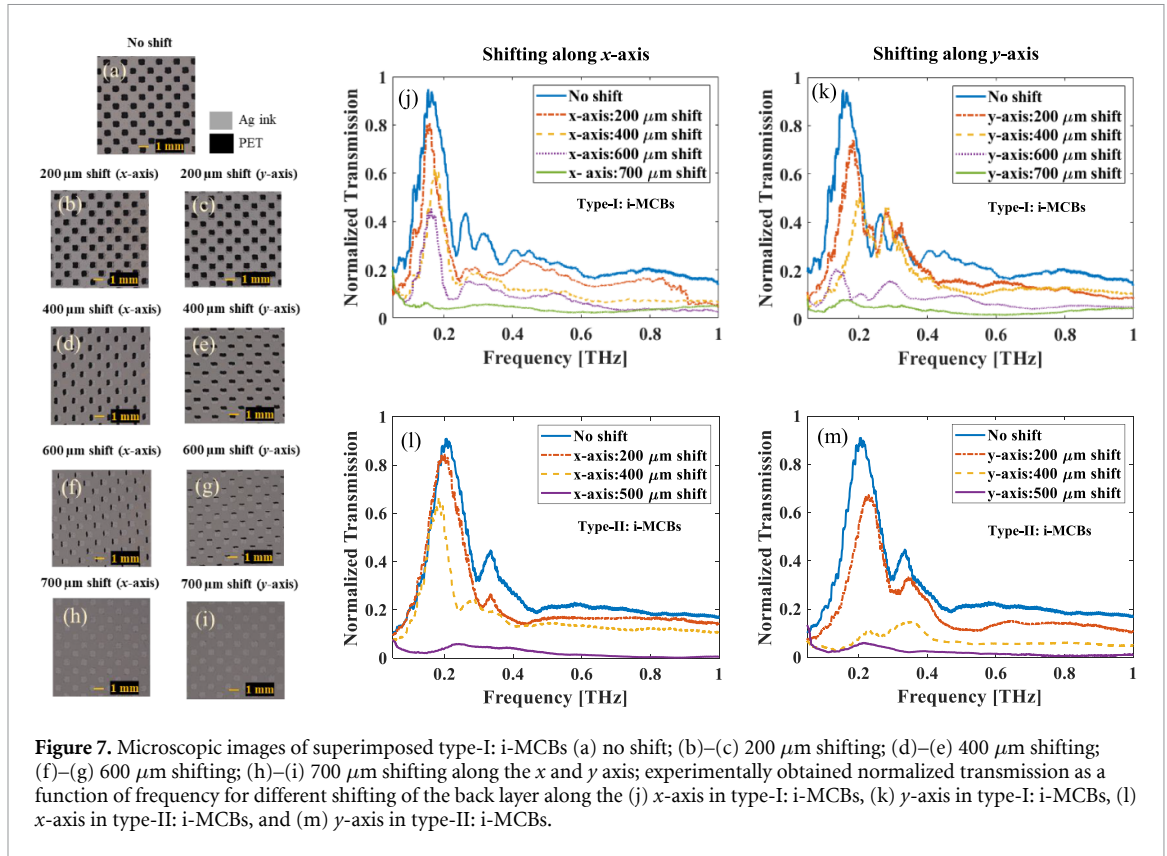
### 3.2.2. Experimental analysis

To corroborate the simulation findings, an experimental analysis was conducted utilizing the continuous-wave THz frequency domain spectroscopy system, as illustrated in figure 4(a), with a specific focus on two identical layers of i-MCB. In line with the simulation data, two identical type-I pattern i-MCB were superimposed. The back layer was systematically shifted along the  $x$  and  $y$ -axis at intervals of 0  $\mu\text{m}$ , 200  $\mu\text{m}$ , 400  $\mu\text{m}$ , 600  $\mu\text{m}$ , and 700  $\mu\text{m}$ , and their corresponding microscopic images are depicted in figures 7(a)–(i), respectively. The layers were aligned such that the printed pattern, created using conductive ink, touched each other, with PET substrates positioned on the outer side of each layer. Also, the corresponding accuracy of the shifting and  $\Delta d_{\text{stacked}}$  of the stacked layers is validated through the microscopic images. These superimposed FSS were then placed between two OAP mirrors in the collimated THz beam path. Based on the experimental analysis, it is noted that for type-I i-MCBs, the NT at 0  $\mu\text{m}$  and 700  $\mu\text{m}$  shifting is 94% and 6%, respectively, at 0.150 THz (refer to figure 7(j)). Additionally, the NT is 80%, 45%, and 38% at 0.150 THz for shifts of 200  $\mu\text{m}$ , 400  $\mu\text{m}$ , and 600  $\mu\text{m}$  along the  $x$ -axis, respectively. Furthermore, when the back layer

was shifted towards the  $y$ -axis, the NT values were observed to be 48%, 22%, 17%, and 7% at 0.150 THz for shifting of 200  $\mu\text{m}$ , 400  $\mu\text{m}$ , 600  $\mu\text{m}$ , and 700  $\mu\text{m}$ , respectively (see figure 7(k)). Similarly, employing two identical type-II i-MCB and shifting along both the  $x$  and  $y$ -axis (refer to figures 7(l)–(m)), the maximum variation in NT for  $x$ -direction shifting was recorded from 90% to 5% at 0.20 THz for a 500  $\mu\text{m}$  shift, as illustrated in figure 7(l). Conversely, for  $y$ -direction moving, the NT was recorded as 58% and 8% for 200  $\mu\text{m}$  and 400  $\mu\text{m}$  shifting.

In the following, NT as a function of shifting along the  $x$  and  $y$ -axis in the case of type-I & II-i-MCBs are plotted in figures 8(a) and (b). The experimental analysis indicates significant variations in NT at the peak center frequency for type-I and type-II i-MCBs, particularly with 700  $\mu\text{m}$  and 500  $\mu\text{m}$  shifting, reaching 88% and 85%, respectively, compared to the no-shift condition. Although overall consistent with simulation results, a minor discrepancy is noted, especially for the 700  $\mu\text{m}$  shift in type-I i-MCBs and the 500  $\mu\text{m}$  shift in type-II i-MCBs. Possible contributing factors include fabrication defects during screen printing, ink spreading, non-uniform block production, varying distances between samples during superimposition, and alignment errors. Mitigating these issues, such as limiting ink spreading and ensuring close alignment between identical samples, could enhance the variation in NT at the operating frequency.

Finally, in table 1, we have compared our proposed work in terms of several design and output parameters with the relevant published works on printed FSS based on flexible substrate. As seen from table 1, our proposed reconfigurable method exhibits



larger variation in transmission at  $f_{\text{opt}}$  as compared to others printed THz FSS. Besides, proposed printed reconfigurable THz i-MCB-FSSs offer a notable advantage: achieving reconfigurability without the need for external stimuli like biasing voltage or photo-excitation. Mechanical shifting, remotely controlled by a motorized translation stage can activate or reconfigure the THz FSS simply as well as accurately. As

shown in figure 2(c), reducing the size of the square non-metallic block shifts the peak center frequency towards higher frequencies, allowing for maximum variation in NT on the higher frequency range of THz. This flexibility in block size selection offers adaptability to specific operating frequency requirements and fabrication capabilities. The peak center frequency could potentially be adjacent to 0.3 THz with an

**Table 1.** Comparison with other relevant published works.

| References | Fabrication method  | Substrate     | Reconfigurability | Modulation depth/variation | Operating frequency |
|------------|---|---------------|-------------------|----------------------------|---------------------|
| [28]       | Flexography   | PET           | Yes               | 41%                        | 0.220 THz           |
| [24]       | Standard lithography, magnetron sputtering metal deposition | Polyimide—STO | Yes               | 40.1%                      | 1.08 THz            |
|            |   |               |                   | 44.7%                      | 1.16 THz            |
| [34]       | Screen-printing   | Kapton, PET   | No                | No                         | 29 GHz<br>60 GHz    |
| [35]       | Screen-printing   | Kapton, PET   | No                | No                         | 60 GHz              |
| [36]       | Screen-printing   | PET           | No                | No                         | 2.4 GHz.            |
| This work  | Screen-printing   | PET           | Yes               | Type-I: 94%–6%             | 0.15 THz            |
|            |   |               |                   | Type-II: 90%–5%            | 0.20 THz            |

i-MCB block size of 300  $\mu\text{m}$  and  $\Delta d$  in accordance with the conventional screen printing meshes with a printing resolution in the range of  $\sim 100$ – $200 \mu\text{m}$ . Subsequently, fine-scale silicon stencils with high printing resolution ( $< 50 \mu\text{m}$ ) [47] could be used for fabricating i-MCB with a peak center frequency of more than 0.3 THz by reducing the block size as well as the gap  $\Delta d$ .

#### 4. Conclusion

In summary, our study involved the analysis and fabrication of THz band-pass filters utilizing screen printing technology for efficient manipulation of THz waves. The reconfigurability aspect was achieved by superposing two i-MCB-patterned THz band-pass filters, requiring the simple shift of one layer along the  $x$  or  $y$ -axis relative to the other. This implementation resulted in significant experimental variations in NT, ranging from 94% to 6% at 0.15 THz and 90% to 5% at 0.20 THz for proposed type-I&II: i-MCBs, respectively. The demonstrated reconfigurable i-MCB printed FSSs hold promise for cost-effective development, opening up avenues for diverse applications such as THz amplitude modulation, spectroscopy, sensing, and imaging.

#### Data availability statements

All data that support the findings of this study are included within the article (and any supplementary files).

#### Acknowledgments

This work was financially supported by NSERC (2023-03322), the Canada Research Chair (CRC-2019-127). As well, Redwan Ahmad is a recipient of the PBEEE doctoral research fellowships (No. 319432) provided by the Fonds de Recherche

du Québec–Nature et Technologies (FRQNT). The authors would like to thank Institut des communications graphiques et de l'imprimabilité, Montreal, QC, Canada for providing a fabrication facility for screen-printed samples.

#### ORCID iDs

Redwan Ahmad  <https://orcid.org/0000-0002-5259-2656>

Ngoc Duc Trinh  <https://orcid.org/0000-0003-3845-3702>

François Blanchard  <https://orcid.org/0000-0002-3335-7458>

#### References

- [1] Ferraro A, Zografopoulos D, Missori M, Peccianti M, Caputo R and Beccherelli R 2016 *Opt. Lett.* **41** 2009–12
- [2] Born N, Reuter M, Koch M and Scheller M 2013 *Opt. Lett.* **38** 908–10
- [3] Tao H, Landy N I, Bingham C M, Zhang X, Averitt R D and Padilla W J 2008 *Opt. Exp.* **16** 7181–8
- [4] Altmann K, Reuter M, Garbat K, Koch M, Dabrowski R and Dierking I 2013 *Opt. Exp.* **21** 12395–400
- [5] Nouman M T, Hwang J H and Jang J H 2016 *Sci. Rep.* **6** 39062
- [6] Anwar R, Mao L and Ning H 2018 *Appl. Sci.* **8** 1689
- [7] Li B, Zeng Y S, Chen B J and Chan C H 2019 *IEEE Trans. Terahertz Sci. Technol.* **9** 510–9
- [8] Yang X, Zeng Y, Liu X, Zhou J, Gan L, Chen H and Yu J 2020 *Microw. Opt. Technol. Lett.* **62** 1860–5
- [9] Poojali J, Ray S, Pesala B, Venkata K C and Arunachalam K 2017 *IEEE Antennas Wirel. Propag. Lett.* **16** 1796–9
- [10] Grossman E N, Dietlein C R and Luukanen A 2006 *Proc. ESA Workshop Millimetre-Wave Technology and Applications* vol 258 pp 353–8 (available at: [www.nist.gov/publications/terahertz-circular-variable-filters](http://www.nist.gov/publications/terahertz-circular-variable-filters))
- [11] Pan W, Huang C, Chen P, Pu M, Ma X and Luo X 2013 *IEEE Trans. Antennas Propag.* **61** 6218–23
- [12] Vegesna S, Zhu Y, Zhao Y, Fan Z, Bernussi A and Saed M 2013 *J. Electromagn. Waves Appl.* **28** 83–90
- [13] Zhai D, Yang Y, Geng Z, Cui B and Zhao R 2018 *IEEE Trans. Terahertz Sci. Technol.* **8** 719–24
- [14] Nauroze S A and Tentzeris M M 2019 *IEEE Trans. Microw. Theory Tech.* **67** 4944–54

- [15] Han J H, Kim I, Ryu J W, Kim J, Cho J H, Yim G S, Park H S, Min B and Choi M 2015 *Opt. Express* **23** 17443
- [16] Li H, Cao Q, Liu L and Wang Y 2018 *IEEE Trans. Antennas Propag.* **66** 1854–62
- [17] Wu L, Zhong S, Huang J and Liu T 2019 *IEEE Trans. Antennas Propag.* **67** 6039–50
- [18] Azemi S N, Ghorbani K and Rowe W S T 2013 *IEEE Antennas Wireless Propag. Lett.* **12** 781–4
- [19] Wu Z, Chen X, Zhang Z, Heng L, Wang S and Zou Y 2019 *Appl. Phys. Express* **12** 057003
- [20] Wen J, Zhao Q, Peng R, Yao H, Qing Y, Yin J and Ren Q 2022 *Opt. Mater. Express* **12** 1461–79
- [21] Akter N, Karabiyik M and Pala N 2019 *IEEE Photonics Conf. (IPC) (San Antonio, TX, USA)* pp 1–2
- [22] Yan R, Arezoomandan S, Sensale-Rodriguez B and Xing H G 2016 *ACS Photonics* **3** 315–23
- [23] Lv X, Ako R T, Bhaskaran M, Sriram S, Fumeaux C and Withayachumnankul W 2022 *IEEE Trans. Terahertz Sci. Technol.* **12** 257–66
- [24] Wang G, Tian H, Wang J, Li S, Guo W and Zhou Z 2021 *Opt. Lett.* **47** 94
- [25] Dong B, Ma H, Wang J, Shi P, Li J, Zhu L, Lou J, Feng M and Qu S 2019 *J. Phys. D: Appl. Phys.* **52** 045301
- [26] Esakkimuthu M, Suseela S B, Sankarajan R, Gupta A and Prabhu S 2019 *J. Electron. Mater.* **48** 2423–9
- [27] Su W, Guo W, Wang Z, Chen P, Gong C, Lin L and Liu W 2019 *J. Phys. D: Appl. Phys.* **52** 095107
- [28] Ahmad R, Zhuldybina M, Ropagnol X, Trinh N D, Bois C, Schneider J and Blanchard F 2023 *Appl. Sci.* **13** 3302
- [29] Zhuldybina M, Ropagnol X, Trudeau C, Bolduc M, Zednik R and Blanchard F 2019 *Sensors* **19** 444
- [30] Zhuldybina M, Beliveau L P, Mansourian M, Ropagnol X, Trinh N D, Bois C and Blanchard F 2021 *46th Int. Conf. on Infrared, Millimeter and Terahertz Waves (IRMMW-thz)* (<https://doi.org/10.1109/IRMMW-THz50926.2021.9566995>)
- [31] Bonnassieux Y et al 2021 *Flex. Print. Electron.* **6** 023001
- [32] Zhuldybina M, Ropagnol X and Blanchard F 2021 *Flex. Print. Electron.* **6** 043007
- [33] Guerboukha H, Amarasinghe Y, Shrestha R, Pizzuto A and Mittleman D M 2021 *Opt. Exp.* **29** 13806–14
- [34] Falade O P, Jilani S F, Ahmed A Y, Wildsmith T, Reip P, Rajab K Z and Alomainy A 2018 *Flex. Print. Electron.* **3** 045005
- [35] Jilani S, Falade O, Wildsmith T, Reip P and Alomainy A 2019 *Appl. Sci.* **9** 945
- [36] Badamchi Z, Trinh N D, Bois C and Djerafi T 2022 *Prog. Electromagn. Res. C* **125** 161–77
- [37] Compton R C, Macfarlane J C, Whitbourn L B, Blanco M M and McPhedran R C 1984 *Opt. Acta* **31** 515–24
- [38] Takano K, Miyamaru F, Akiyama K, Miyazaki H, Takeda M W, Abe Y, Tokuda Y, Ito H and Hangyo M 2014 *Opt. Express* **22** 24787
- [39] Nakata Y, Fukawa K, Nakanishi T, Urade Y, Okimura K and Miyamaru F 2019 *Phys. Rev. Appl.* **11** 044008
- [40] Dawes D H, McPhedran R C and Whitbourn L B 1989 *Appl. Opt.* **28** 3498
- [41] Higashira T, Kageyama T, Kashiwagi K, Miyashita H, Takano K, Nakajima M and Lee S S 2017 *J. Infrared Millim. Terahertz Waves* **38** 1098–106
- [42] Kondo T, Nagashima T and Hangyo M 2003 *Jpn. J. Appl. Phys.* **42** 4A
- [43] Nakata Y, Urade Y, Nakanishi T and Kitano M 2013 *Phys. Rev. B* **88** 20
- [44] Zhuldybina M, Ropagnol X, Bois C, Zednik R J and Blanchard F 2020 *npj Flex. Electron.* **4** 1
- [45] Jackson J D 1999 *Classical Electrodynamics* 3rd edn (Wiley)
- [46] LCF® 4000 Clear Polyester (available at: <https://multi-plastics.com/products/lcf-4000-clear-polyester/>) (Accessed 25 February 2024)
- [47] Hyun W J, Lim S, Ahn B Y, Lewis J A, Frisbie C D and Francis L F 2015 *ACS Appl. Mater. Interfaces* **7** 12619–24